Emergence of inertia in the low-Reynolds regime of self-diffusiophoretic motion

Emmy N. Zero[*] and Vincent H. Crespi[†]
Department of Physics, The Pennsylvania State University, University Park, Pennsylvania 16802, USA

(Received 28 April 2022; revised 7 September 2023; accepted 6 November 2023; published 8 May 2024)

For isotropic swimming particles driven by self-diffusiophoresis at zero Reynolds number (where particle velocity responds instantaneously to applied force), the diffusive timescale of emitted solute can produce an emergent quasi-inertial behavior. These particles can orbit in a central potential and reorient under second-order dynamics, not the first-order dynamics of classical zero-Reynolds motion. They are described by a simple effective model that embeds their history-dependent behavior as an effective inertia, this being the most primitive expression of memory. The system can be parameterized with dynamic quantities such as particle size and swimming speed, without detailed knowledge of the diffusiophoretic mechanism.

DOI: 10.1103/PhysRevE.109.054602

I. INTRODUCTION

Memory is commonly associated with hysteresis, where past events set state variables that control the current dynamics, as in a simple ferromagnet or a complex emergent system. At a more rudimentary level, inertia can also be thought of as an expression of memory: To predict the future of a second-order mechanical system, we need both the present configuration and its derivative in time, i.e., the minimal possible dependence on past behavior. Motion at very low Reynolds number lacks inertia and thus leaves a system with no memory: Only the present matters for the future of a system governed by a first-order equation of motion, and motion immediately stops in the absence of external drive. But microscopic dynamics that go beyond hydrodynamics to include, for example, the diffusion of chemical species can introduce new timescales and recover inertialike effects even at zero Reynolds number.

Consider, for example, an object that moves with a constant velocity once set into motion that can follow uniform circular orbits around an attractive central potential, and for which external forces transverse to its direction of motion produce an acceleration in the direction of the external force. These characteristics are familiar from classical mechanics without dissipation; here we show that they can also be achieved *at zero Reynolds number* for self-diffusiophoretic systems in which the slow dissipation of chemical gradients (associated with internally generated propulsive forces) can introduce enough memory to recover certain inertial features of finite-Reynolds motion.

[*]emmy@psu.edu
[†]vhc2@psu.edu

Several such systems—active particles driven by a self-maintained chemical gradient while lacking any intrinsic orientation—have been realized experimentally [1,2]. To sustain motion, they spontaneously break symmetry through either mutable surface properties or the chemical gradient itself. Such systems span scales from centimeters to nanometers and employ a variety of mechanisms to maintain nonequilibrium gradients. In oil-water-surfactant emulsions, droplets of an immiscible fluid in a surfactant-rich continuous phase are driven to motion by a surface tension gradient that can arise from chemical reactions between reactants inside and outside the droplet [3,4], solubilization of the droplet's contents into surfactant micelles in the bulk [5–8], or the droplet catalyzing a reaction in the bulk [9,10]. Similar behavior has been observed in droplets at liquid-air [11] and liquid-glass interfaces, driven by surfactant gradients at those interfaces [1], going back to at least 1888 [12,13]. The polymerization of ubiquitous monomers can generate similar behavior in the bacterium *Listeria* and enzyme-coated microspheres [14]. Many of these systems have a finite timescale associated with the accommodation of the degrees of freedom describing the gradient field to changes in the environment through which the particle moves.

A minimal model should capture two essential physical processes: The continuous emission of diffusing solute and the particle motion that arises from the local gradient of this solute. The detailed chemical interaction between a particle and its environs is subsumed into the sensitivity of the propulsive force to this gradient, while the fluid flow around the particle is subsumed into an assumption of low Reynolds number motion. Simulations and analysis show that this model is best described as a history-dependent dynamical system, with the degree of history dependence characterized by the system's Péclet number. This simplified model complements more detailed treatments which consider the flow fields within and around a spherical particle, and advective transport of the solute [2,15].

Consider a particle with position $\boldsymbol{r}$ and radius a, as shown in Fig. 1. Rather than as a hard sphere, the particle interacts

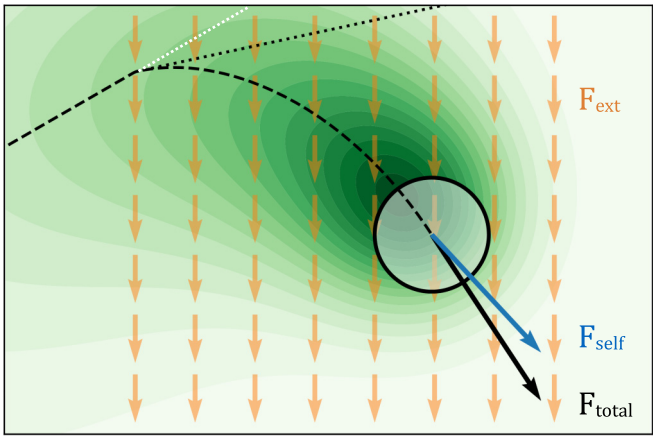

FIG. 1. A gradient-driven solute-emitting active particle enters a region of constant force in the $-\boldsymbol{y}$ direction. Solute density is shown in green. At high Péclet number, the particle leaves behind a lingering trail of solute. At low Reynolds number, the particle's velocity responds instantaneously, as shown by the black dotted tangent line, but this also initiates a gradual change in self-diffusophoretic force, causing the trajectory to curve towards an eventual steady-state direction of motion. Shown with $P = 2.0$.

with the environment as a Gaussian with variance a^2. It emits solute at a fixed (unit) rate, which then diffuses at D_0 to obtain a concentration profile ρ:

$$\frac{\partial \rho}{\partial t} = D_0 \nabla^2 \rho + N^3(\boldsymbol{r}, a). \tag{1}$$

$N^3(\boldsymbol{r}, a)$ denotes a 3D normal distribution with mean $\boldsymbol{r}$ and variance a^2. A system with sensing and emitting profiles of the same variance is equivalent to one that emits with twice the variance and senses at a single point (for convenience, we implement the latter form). We assume that the particle experiences a repulsive diffusiophoretic force $\boldsymbol{F}_{\text{self}}$ proportional to the negative gradient of ρ, again averaged over a Gaussian of width a. For a particle located at $\boldsymbol{r}$, this is

$$\boldsymbol{F}_{\text{self}}(\boldsymbol{r}, \rho) = -\mu \int_0^\infty \nabla \rho(\boldsymbol{x}) \cdot N^3(\boldsymbol{x} - \boldsymbol{r}, a) d\boldsymbol{x}. \tag{2}$$

μ represents the sensitivity of the diffusiophoretic force to the solute gradient. In the Stokes regime ($\text{Re} = 0$), the particle's velocity is proportional to the force upon it. Combining all other forces into $\boldsymbol{F}_{\text{ext}}$ (which could include external potentials, Brownian fluctuations, and forces from nearby particles), its motion is governed by

$$\frac{d\boldsymbol{r}}{dt} = \boldsymbol{F}_{\text{self}}(\rho) + \boldsymbol{F}_{\text{ext}}. \tag{3}$$

When $\boldsymbol{F}_{\text{ext}}$ is zero, the parameters a, μ, and D_0 characterize the system, representing the particle's size, its gradient sensitivity, and the solute's diffusivity, respectively. In Sec. III, we derive an expression for an isolated particle's steady-state velocity $v(\mu, a, D_0)$ in terms of these three parameters. That, in turn, allows us to combine these three parameters into a dimensionless Péclet number $P = va/D_0$ which characterizes the strength of memory effects in the system.

Figure 1 illustrates how one such particle responds to an abrupt change in the external force. Contours of the solute cloud (shown in green) remember the particle's recent trajectory, drawn as a dashed line. As described in Appendix A, we can formalize this relationship between solute trajectory $\rho(x, t)$ and particle history $\boldsymbol{r}(t' \leqslant t)$ using the Green's function of the diffusion equation [16]. Doing so lets us recast Eqs. (1)–(3) in a delay-differential form

$$\frac{d\boldsymbol{r}}{dt} = \mu \int_0^\infty \mathcal{F}(\boldsymbol{r} - \boldsymbol{r}_\tau, \tau) d\tau + \boldsymbol{F}_{\text{ext}} \tag{4}$$

where $\mathcal{F}(\boldsymbol{r} - \boldsymbol{r}_\tau, \tau)$ represents the the gradient sensed by a particle at $\boldsymbol{r}$ due to the solute emitted at the position $\boldsymbol{r}_\tau$ a time τ ago, given by

$$\mathcal{F}(\boldsymbol{x}, \tau) \equiv N^3(\boldsymbol{x}, \sqrt{2D_0\tau + 2a^2}) \frac{\boldsymbol{x}}{2D_0\tau + 2a^2}. \tag{5}$$

Equation (4) allows us to simulate particle motion in an infinite domain, establish the speed of steady-state motion in terms of μ, D_0, and a, and reproduce the bifurcation with increasing motility μ found in Refs. [2,10]. Finally, Eq. (4) hints at the origin of the memory that is visible in the slow reorientation of Fig. 1—the particle's motion is dictated by its displacement over the recent past. Our focus is the mechanism for the emergence of quasi-inertial phenomena from the underlying microscopic degrees of freedom that "dress" the particle's macroscopic motion.

II. RANDOM HILLSCAPE

The trajectory shown in Fig. 1 illustrates how this system responds to a time-varying external force. Upon experiencing a sudden change in $\boldsymbol{F}_{\text{ext}}$, the particle's velocity immediately adjusts, as expected for a zero-Reynolds system. But this also begins a slower process in which the particle's self-diffusiophoretic force rotates into alignment with $\boldsymbol{F}_{\text{ext}}$, as its diffusive cloud gradually adjusts to the new conditions of motion. Clearly, we need to go beyond steady-state solutions to understand the dynamics of Eqs. (1)–(3). To do so we'll move to numerical simulations based on Eq. (4). This allows us to see how our system will respond to environments or stimuli, defined, respectively, by position- and time-dependent $\boldsymbol{F}_{\text{ext}}$[1]. In particular, we will focus initially on motion in a *random hillscape*, in hopes that generic behavior in a random potential may reveal hidden simplicities within the delay-differential formalism.

The random potential landscape is composed of 49 plane waves

$$U_{\text{hills}}(\boldsymbol{x}) = M \sum_{m=1}^{49} A_m |\boldsymbol{k}_m|^{-3/2} \exp(i\boldsymbol{k}_m \cdot \boldsymbol{x}) \tag{6}$$

with $\boldsymbol{k}_m \sim N^2(0, \sigma_k)$ and $|A_m| \sim N(0, \sigma_A)$, which results in an aperiodic force field defined everywhere in space. M is chosen to fix the spatially averaged value of $|\boldsymbol{F}_{\text{ext}}|^2$ relative to the self-diffusiophoretic force, while σ_k determines the characteristic length scale of the hillscape. An example is shown in Fig. 2 [17].

[1]In addition to external forces, $\boldsymbol{F}_{\text{ext}}$ could represent the diffusiophoretic force due to solute gradient from other particles' emissions in a multiparticle system.

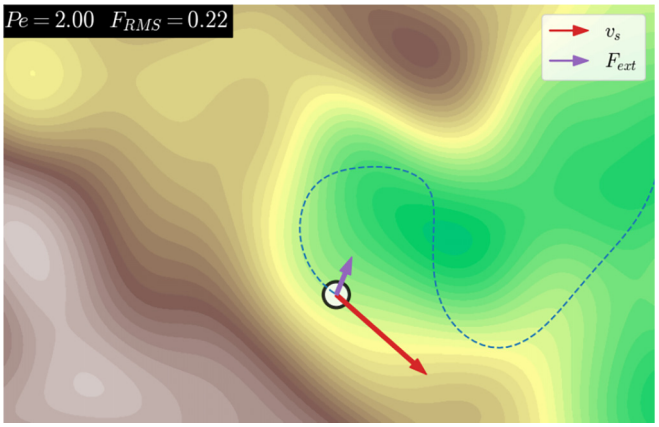

FIG. 2. Trajectory of a particle moving in a random, lumpy potential, with self-propulsion v_s and external force $\boldsymbol{F}_{\text{ext}}$ illustrated. This is a stronger version of the environment shown in Fig. 3, and has $P = 2.00$. Full animation is shown in the Supplemental Material [17].

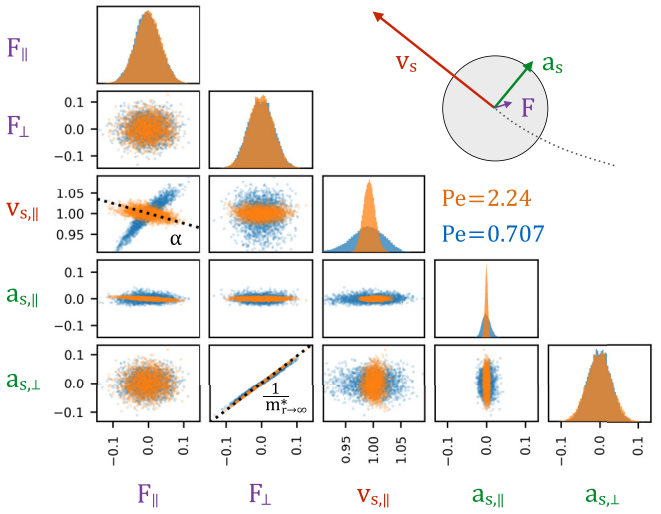

FIG. 3. Analysis of trajectories for simulated particles moving in a random potential, as shown in Fig. 2. Diagonal shows histograms of the particle's autophoretic velocity $\boldsymbol{v}_s$ (red), its derivative $\frac{d}{dt}\boldsymbol{v}_s = \boldsymbol{a}_s$ (green), and the droplet's velocity due to the potential gradient $\boldsymbol{F}_{\text{ext}}$ (purple). Off-diagonal scatter-plots show all pairwise combinations. The unit vector $\hat{e}_\parallel$ is defined to always be parallel with $\boldsymbol{v}_s$. The tight linear correlation between the $\hat{e}_\perp$ components of $\boldsymbol{F}_{\text{ext}}$ and $\boldsymbol{a}_s$ suggest a simplified model where the droplet and its cloud 'turn' gradually to align with the external force.

To analyze the resulting behavior, we will initially affect ignorance of the diffusiophoretic nature of the system. We observe $\boldsymbol{F}_{\text{ext}}$, the known environmental force acting on the particle, and $\boldsymbol{v}$, the particle's velocity. Knowing that this motion exists at zero Reynolds number, we say that there is a deficit in the force needed to explain the observed motion, which we define as

$$\boldsymbol{v}_s \equiv \boldsymbol{v} - \boldsymbol{F}_{\text{ext}}, \tag{7}$$

with s standing for self. Our job then is to explain the dynamics of $\boldsymbol{v}_s$ in response to $\boldsymbol{F}_{\text{ext}}$, so we define $\boldsymbol{a}_s \equiv \frac{d}{dt}\boldsymbol{v}_s$.

To this end, we analyze two scenarios with different Péclet numbers, $P = 2.24$ and $P = 0.707$, both moving in the same random potential with $\text{RMS}(\boldsymbol{F}_{\text{ext}}) = 0.1v_s$ and $2\pi/\sigma_k = 20a$. The *scatter-plot matrix* in Fig. 3 displays both distributions of individual dynamical variables and correlations between pairs thereof. The vectors $\boldsymbol{F}_{\text{ext}}$, $\boldsymbol{v}_s$, and $\boldsymbol{a}_s$ are projected onto a basis which tracks $\boldsymbol{v}_s$. This choice of basis helps elucidate how the sensed chemical gradient (and its effect on particle motion) responds to external stimulus in the form of $\boldsymbol{F}_{\text{ext}}$. Because $a_{s\parallel}$ and v_s can be combined to track the rotation of the basis vectors, no information is lost by the projection. The total velocity of the particle is the sum of $\boldsymbol{F}_{\text{ext}}$ and $\boldsymbol{v}_s$.

Subplots on the diagonal of Fig. 3 are histograms of each component's value across the time series. The first two histograms show that particles in both ensembles experience similar $\boldsymbol{F}_{\text{ext}}$ despite a threefold difference in P. The third, showing the magnitude of the self-diffusiophoretic force $\boldsymbol{v}_{s\parallel}$, indicates that while both low- and high-Péclet particles both maintain an autophoretic force around the nominal $\boldsymbol{v}_s = 1.0$, the high-Péclet system's sensed gradient is much less variable. This can be understood as the result of the sign change in (9)—beyond $P \approx 1.258$, an increase in total speed will cause the particle to outrun its own cloud. A similar effect is seen in the distribution of $\boldsymbol{a}_{s\parallel}$. Finally, for both Péclet numbers, the observed distributions of $\boldsymbol{a}_{s\perp}$ are approximately Gaussian with $\sigma \approx 0.032$, indicating a turning radius rarely tighter than $15a$.

The off-diagonal plots scatter one component against another, demonstrating correlations between the pairs of variables; we will first highlight, and subsequently explain, the most notable combinations. Since our goal is to understand the evolution of $\boldsymbol{v}_s$, the most interesting of these are the two leftmost columns, which show the response of $\boldsymbol{v}_s$ and its derivative $\boldsymbol{a}_s$ to the external force. Both $a_{s,\perp}$ vs $F_\parallel$ and $a_{s,\parallel}$ vs $F_\perp$ are nearly independent. In the first column, $v_{s,\parallel}$ vs $F_\parallel$ shows that the sensed gradient tracks the parallel component of $\boldsymbol{F}_{\text{ext}}$. It also explains the difference in the variance of $\boldsymbol{a}_{s,\parallel}$ across the two cases, as the correlation is strongly positive in the low-Péclet case and weakly negative in the high-Péclet case. Most striking is the plot of $a_{s,\perp}$ vs $F_\perp$, *which shows near-perfect correlation* in both high- and low-Péclet cases. The dotted lines derive from a linear response analysis described in Sec. III (and explained more fully in Appendix B).

Taken together, these observations suggest the existence of a low-dimensional approximation of the system—although the solute cloud surrounding a particle may be infinite-dimensional, the plausibly accessible shapes of this cloud (and their effects on particle motion) can mostly be described by one or two variables (an orientation and/or a velocity). Abstracting away the cloud, the existence of a linear relationship between $a_{s,\perp}$ and $F_\perp$ suggests that the dynamics transverse to $\boldsymbol{v}_s$ develop characteristics of an inertia—at zero Reynolds number—due to the separation in timescales between the dynamics of the cloud and the dynamics of the motor within.

III. LINEAR AND CIRCULAR STEADY-STATE MOTION

The simulations described in Sec. II showed how an external force can affect a droplet's swimming velocity $\boldsymbol{v}_s$: The parallel component of $\boldsymbol{F}_{\text{ext}}$ causes a shift in its swimming speed and the perpendicular component will induce acceleration in that direction, even at zero Reynolds number, due to

the sluggish response of the solute cloud. To sharpen this notion, we'll examine two steady-state solutions to Eq. (4). The first, linear motion, establishes a droplet's nominal swimming speed v_0 and its response to a weak, parallel $\boldsymbol{F}_{\text{ext}}$. The second, uniform circular motion with a centripetal force, centers perpendicular force and acceleration in the familiar Newtonian circumstance of orbits in a central potential.

Our approach in both cases (detailed more fully in Appendix B) is to posit a trajectory $\boldsymbol{r}(t)$ which yields a constant environment for the particle in its own frame of reference. This gives explicit, constant values for both the particle's speed $d\boldsymbol{r}/dt$ and for the diffusiophoretic force, in integral form, via the right-hand side of Eq. (4). What remains is to find parameters of the system (μ, D_0) and trajectory (speed, orbital radius) which make the hypothesis self-consistent.

For linear motion, the hypothesis $\boldsymbol{r} = \boldsymbol{v}t$ on the right-hand side of Eq. (4) can be evaluated exactly, giving a relation between motility μ and speed v which can be used to find the nominal swimming speed v_0 for a given system and perturbations to swimming speed in the presence of a constant external force $\alpha \equiv (d\boldsymbol{v}/d\boldsymbol{F}_{\text{ext}} - 1)$[2]:

$$\mu(P) = 8\pi D_0^2 a \frac{P^2\left(P - \frac{a}{D_0}\boldsymbol{F}_{\text{ext},\parallel}\right)}{\frac{2}{\sqrt{\pi}}P - (P^2-1)\text{erfcx}(P) - 1}, \tag{8}$$

$$\alpha = \frac{\frac{2P}{\sqrt{\pi}} - (P^2-1)\text{erfcx}(P) - 1}{\frac{2P}{\sqrt{\pi}}(3-P^2) + (2P^4 - 3P^2 + 3)\text{erfcx}(P) - 3} - 1, \tag{9}$$

with $P \equiv va/D_0$. Taking the limit of Eq. (8) as $P \to 0^+$ also yields a critical μ_c below which no motion occurs, reproducing the bifurcation found in Refs. [2,8]. This result allows the model to be parameterized by its swimming speed rather than the less easily observed μ.

We use a similar approach for circular orbits, positing a trajectory with radius R and then finding the requisite angular velocity ω and external force necessary to sustain it. Such a trajectory has velocity $d\boldsymbol{r}/dt = R\omega\hat{e}_\theta$ and time-delayed displacement:

$$\boldsymbol{r} - \boldsymbol{r}_\tau = R(1 - \cos(\omega\tau))\hat{e}_r + R\sin(\omega\tau)\hat{e}_\theta. \tag{10}$$

These can be plugged into Eq. (4) to produce an integral equation in terms of R and ω which can be solved numerically to find ω as a function of R, parameterized by μ (or, equivalently, by the intrinsic speed $v_0 = \lim_{R\to\infty} R\omega$). The tangential component of the sensed gradient ($F_\parallel$) is sufficient to fix ω. With that it is straightforward to calculate the radial component of the diffusiophoretic force ($F_\perp$), and from there the centripetal $\boldsymbol{F}_{\text{ext}}$ needed to counteract it. The upper-left subplot of Fig. 4 shows the resulting radial and tangential components of the diffusiophoretic force $\boldsymbol{F}_{\text{self}}$ generated by a circular orbit with radius R and the self-consistent angular velocity $\omega = \boldsymbol{F}_\parallel/R$, spanning a range from tight circles that are smaller than the droplet itself at $R < a$ to very gently curved trajectories at $R \gg a$.

[2]One interesting feature of Eq. (9) is that α changes signs as P increases, that is, depending on the system's parameters (μ, D_0, and a) an external force may have a smaller or larger effect on the speed of a droplet than it would on a passive particle of the same size.

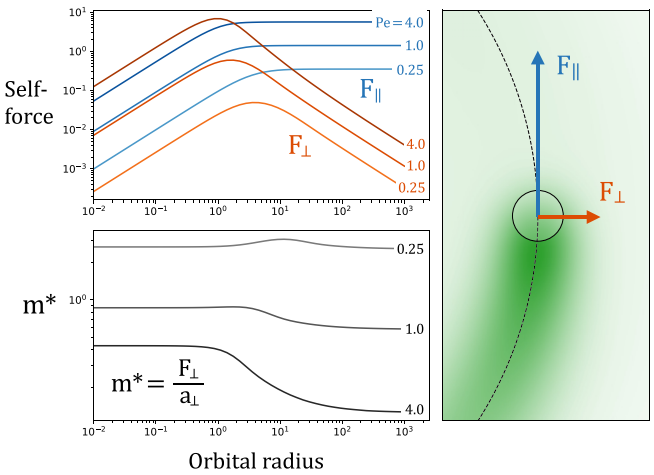

FIG. 4. Top left: Components of self-diffusiophoretic force for self-powered circular motion as a function of radius, shown for three values of Pe with different terminal velocities. Bottom left: Effective mass m^*, the ratio of constraining force and centripetal acceleration, which approaches a constant in both large- and small-R limits. Right: Circular orbit ansatz trajectory with resulting cloud and gradient.

These curves have simple asymptotic behaviors in both the $R \to 0$ and $R \to \infty$ limits. For $R \gg a$, $\boldsymbol{F}_\parallel$ approaches the straight-line result while the requisite centripetal force $-\boldsymbol{F}_\perp$ scales as R^{-1}. In the $R \ll a$ limit, the external force $\boldsymbol{F}_\perp$ takes the form of a harmonic potential. The tangential $\boldsymbol{F}_\parallel$ also scales linearly with R, meaning the orbital period approaches a constant, as with the familiar harmonic oscillator. It is interesting that the ratio of centripetal force $-\boldsymbol{F}_\perp$ to centripetal acceleration approaches a *constant* in both limits, allowing definition of a curvature-dependent inertia $m^\star$ shown in the lower-left subplot of Fig. 4. This quantity, in the $R \to \infty$ limit, dictates the slope of the dotted trendline in the $a_{s,\perp}$ vs $F_\perp$ subplot of Fig. 3. The $F_\perp$ curves in Fig. 4 also represent, for a given motility μ, the centripetal force needed to permit an orbit with radius R. This could, in principle, be used to construct a central potential which would permit orbits of any radius. Although numerical simulations of single particles in such a potential show that these orbits are not long-time stable and tend to either collapse to a small radius or escape to infinity, introduction of a modest corrugation to the radial dependence of the external force can stabilize circular orbits at a relatively dense set of local minima. The ability to define a useful concept of effective mass in the time-honored regime of a radial central potential underlines the manner in which the new timescale associated with the finite Péclet number of these powered particles can reintroduce a measure of inertia-like behavior into an Re = 0 system.

IV. EMERGENT QUASI-INERTIAL MODEL

Equations (1) and (3) define a dynamical system with an infinite-dimensional state space, but the clear structure visible in Fig. 3 and its similarity to steady-state solutions suggest that a much simpler description might be found. We can use a physical intuition and the history-dependent form of Eq. (4) to justify such a model. The influence of a particle's delayed

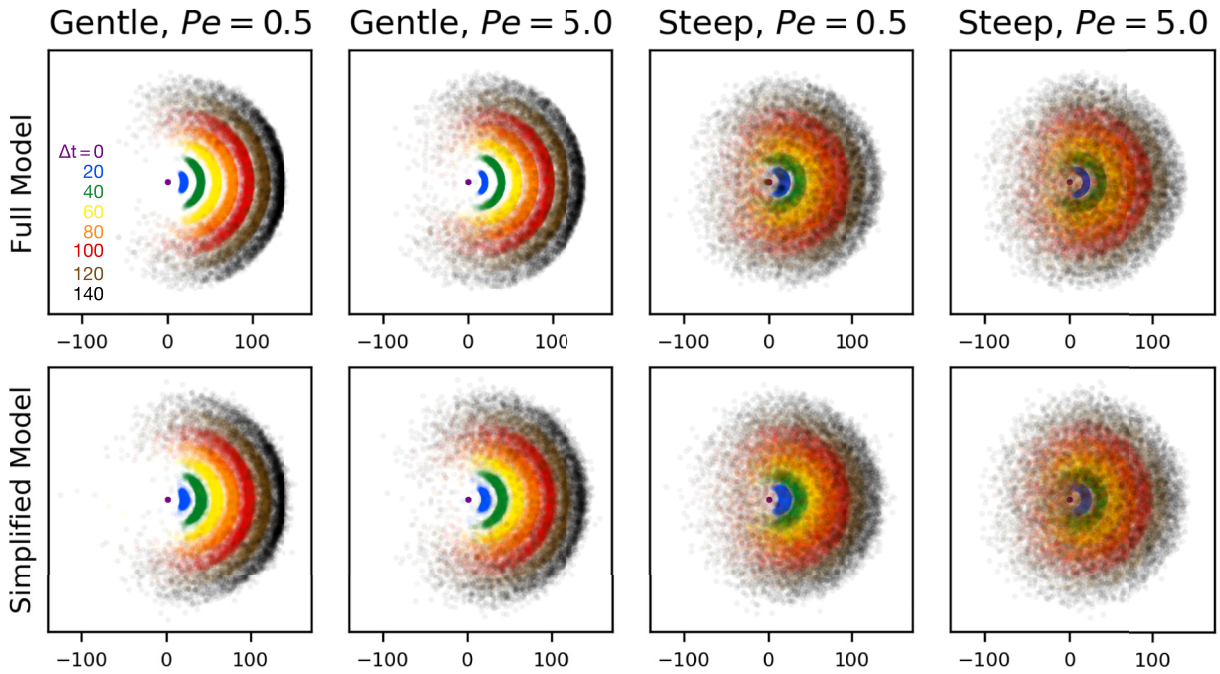

FIG. 5. Comparison of full and simplified models for two Péclet numbers (0.5 and 5.0) and two magnitudes of the external potential (gentle and steep). Each plot shows the displacements of an ensemble of particles conditioned on traveling in the $+x$ direction at $\Delta t = 0$, over a color-coded succession of time intervals. Together they approximate the evolving probability density of a particle's position, starting from a delta function. (The red dot in the steep, low-Péclet subplot is the result of a single trajectory falling into a limit cycle with a period close to 100, like that shown in the Supplemental Material [17]).

displacement $\boldsymbol{r} - \boldsymbol{r}_\tau$ on its current motion $\dot{\boldsymbol{r}}$ has two time horizons—the diffusion time a^2/D_0 and the traversal time a/v of the particle's characteristic size. Emissions older than a few times either of these spans will have a negligible effect on the present velocity. Thus, rather than knowing the full history $\boldsymbol{r}(t' < t)$, it is sufficient to know only the recent past. Thus, it is reasonable to expand $\boldsymbol{r}_\tau$ as a series in τ. Assuming a sufficiently weak and smooth $\boldsymbol{F}_{\rm ext}$, we can expand $\boldsymbol{r}$ to second order, approximating the history in Eq. (4) through only the velocity and acceleration. In fact, the results of Sec. III give us a relation between $\dot{\boldsymbol{r}}$, $\ddot{\boldsymbol{r}}$, and $\boldsymbol{F}_{\rm ext}$ in the case where higher terms vanish in the moving frame of reference.

This produces a model with the same form as an active Brownian particle [18] (ABP), which has an explicit orientation, here played by the local negative gradient of $\rho(\boldsymbol{r})$. Unlike simple ABPs, the external force $\boldsymbol{F}_{\rm ext}$ enters twice—both as a direct contributor to $d\boldsymbol{r}/dt$ and as a *torque* which gradually rotates the orientation $\tilde{F}_{\rm self}$. Denoting $\hat{e}_\parallel$ as the unit vector parallel to $\tilde{F}_{\rm self}$, and $\hat{e}_\perp$ as perpendicular to that, the simplified equations of motion become

$$v_s = v_0 + \alpha(\boldsymbol{F}_{\rm ext} \cdot \hat{e}_\parallel), \tag{11}$$

$$\frac{d}{dt}\boldsymbol{r} = v_s \hat{e}_\parallel + \boldsymbol{F}_{\rm ext}, \tag{12}$$

$$\frac{d}{dt}\hat{e}_\parallel = \frac{1}{m^\star_\infty v_0}(\boldsymbol{F}_{\rm ext} \cdot \hat{e}_\perp)\hat{e}_\perp. \tag{13}$$

That is, the simplified droplet has an intrinsic orientation $\hat{e}_\parallel$ and an autophoretic speed v_s. Its total velocity [Eq. (12)] is the sum of its self-propulsion $v_s\hat{e}_\parallel$ and the external force $\boldsymbol{F}_{\rm ext}$. The intrinsic speed [Eq. (11)] has a nominal value of v_0, with a correction from the parallel component of $\boldsymbol{F}_{\rm ext}$, which reflects the shift derived in Eq. (B9). Finally, the orientation $\hat{e}_\parallel$ [Eq. (13)] rotates in response to the perpendicular component of $\boldsymbol{F}_{\rm ext}$, with a motility $(m^\star v_0)^{-1}$ derived in Eq. (B18), i.e., it has an emergent inertia.

To test the simplified system governed by Eqs. (11)–(13), we prepared 100 separate realizations of the random hillscape potential, each scaled to two separate amplitudes (force RMS of 0.04 and 0.08) and tested at two different values of Péclet number (0.5 and 5.0). For each of these, we simulated both the full and simplified models with identical initial conditions. The resulting trajectories are compared by examining the short-term displacements as shown in Fig. 5. For example, a red point indicated the displacement after an interval of $\Delta t = 100$, relative to its direction of travel at $\Delta t = 0$. Each subplot has 5000 such points, taken at intervals of 200 from 100 different random potentials. These have the effect of illustrating the short- to medium-term statistical behavior of both models. Comparing the full and simplified models, it is clear that the instantaneous model with inertia and explicit orientation closely reproduces the near-term evolution of the full model across a twofold range of (relatively weak) external forces and a tenfold range in Péclet number.[3]

The close correspondence between the full and simplified models in Fig. 5 demonstrates that we can effectively bridge

[3]In the steep, low-Péclet case, certain trajectories for the true system get trapped in a local minimum as indicated by the dark red dot near the origin. This cannot be reproduced in the simplified model, which does not allow for particles to be stationary when $\boldsymbol{F}_{\rm ext} = 0$.

from the microscopic chemical details embodied by μ to the motility constants v_0, α, and $m^\star_\infty$ in the ODE approximation and, in turn, map the full self-diffusiophoretic system onto familiar, computationally inexpensive phenomenological models of oriented dry active matter with Vicsek or ABP-type state variables [18]. Memory-dependent phenomena seen in single or few-particle systems such as flip-flopping demultiplexing branched channels that exploit trail avoidance [6], microfluidic Newton's cradles [19], and directional persistence transitions in self-propelled droplets [20–23] can thereby be connected to larger-scale behaviors such as flocking and swarms [18] that are more typically treated with higher-level effective models.

Although the numerical experiments in Figs. 3 and 5 considered single-particle trajectories in a potential, the most interesting source of $\boldsymbol{F}_{\text{ext}}$ is the gradient from other particles. Such multiparticle systems can be examined in both the full and simplified models, the latter buoyed by the low computational cost of first-order N-body dynamics. More broadly, the emergence of the rudiments of inertia from a dynamics of underlying microscopic degrees of freedom that also drives particle motility and interparticle interactions provides a rich landscape for exploring the interplay of time-delayed interactions, memory, and inertia, such as unidirectional vibrational modes within crystallized arrays of comoving particles that break Galilean invariance and other behaviors.

ACKNOWLEDGMENT

This work was supported by the National Science Foundation through the Penn State Materials Research Science and Engineering Center under Awards No. DMR-1420620 and No. DMR-2011839.

APPENDIX A: TRANSFORMATION TO DELAY EQUATIONS

In the main text, we described a system which couples the motion of a particle to the gradient of a diffusive species which the particle itself emits. Here we describe how the proposed mechanism of emission, diffusion and gradient sensing can be recast into a delay-differential equation. In the following, $\star$ will denote a convolution *in position only* as described in Table I. Convolutions in time will be stated explicitly.

Our system is defined by two state variables, $\boldsymbol{r}$, the position of the particle, and $\rho(\boldsymbol{x})$, the density of emitted solute. The evolution of ρ is governed by diffusion and emission

$$\left(\frac{d}{dt} - D_0\nabla^2\right)\rho = N^3(\boldsymbol{x}-\boldsymbol{r}, a). \tag{A1}$$

Neglecting the dynamics of $\boldsymbol{r}$, (A1) is the venerable heat equation with a moving Gaussian source. It can be solved using the Green's function of the diffusion operator $\partial_t - D_0\nabla^2$,

$$G(\boldsymbol{x}, t) = \theta(t)\left(\frac{1}{4\pi D_0 t}\right)^{3/2} e^{-x^2/4D_0 t} \tag{A2}$$

$$= \theta(t)N^3(0, \sqrt{2D_0 t}), \tag{A3}$$

which is simply a 3D Gaussian with a variance growing at rate $2D_0$, and describes the evolution of a pointlike (δ^3) emission.

Given the emitter's history $\boldsymbol{r}(t' < t)$, we can find $\rho(x, t)$ by convolving G with the emission profile N^3, translated by $\boldsymbol{r}$:

$$\rho(\boldsymbol{x}, t) = \int_{-\infty}^{t} dt' \int_{\mathbb{R}^3} d\boldsymbol{x}' G(\boldsymbol{x}-\boldsymbol{x}', t-t')N^3(\boldsymbol{x}'-\boldsymbol{r}(t'), a). \tag{A4}$$

Happily, the spatial part of this convolution can be expressed by advancing the time argument of G. That is,

$$G(\boldsymbol{x}, t) \star N^3(0, a) = G\left(\boldsymbol{x}, t + \frac{a^2}{2D_0}\right), \tag{A5}$$

so

$$\rho(\boldsymbol{x}, t) = \int_{-\infty}^{t} dt' G\left(\boldsymbol{x}-\boldsymbol{r}(t'), t-t' + \frac{a^2}{2D_0}\right). \tag{A6}$$

The second half of this system defines how the movement of $\boldsymbol{r}$ is affected by ρ. Again assuming a Gaussian profile, we define a force which is proportional to the gradient of ρ averaged over a Gaussian of width a:

$$\boldsymbol{F}_{\text{self}}(\boldsymbol{r}, \rho) = -\mu(\nabla\rho(\boldsymbol{x}) \star N^3(\boldsymbol{r}-\boldsymbol{x}, a)). \tag{A7}$$

This is again a spatial convolution and the sensing profile can again be absorbed into the integrand. Combining Eqs. (A6) and (A7), we can construct an expression for $\boldsymbol{F}_{\text{self}}$ purely in terms of $\boldsymbol{r}(t' < t)$. We define a force kernel $\mathcal{F}(\boldsymbol{x}, \tau)$ which describes *the force on a particle from solute emitted a distance* $\boldsymbol{x}$ *away and time* τ *ago*:

$$\mathcal{F}(\boldsymbol{x}, \tau) \equiv \mu N^3(\boldsymbol{x}, \sigma_\tau)\frac{\boldsymbol{x}}{\sigma_\tau^2}, \tag{A8}$$

TABLE I. Symbol definitions.

Symbol	Definition	Description
$\boldsymbol{r}$		Particle position
$\boldsymbol{x}$		A point in space
τ		A delay. Units of time, $\geqslant 0$
z_τ	$z(t-\tau)$	Value of z at time $t-\tau$
$N^3(\boldsymbol{x}, \sigma)$	$\frac{1}{(2\pi\sigma^2)^{\frac{3}{2}}}\exp(-\frac{1}{2}(\frac{x}{\sigma})^2)$	A 3D Gaussian with variance σ, evaluated at $\boldsymbol{x}$
σ_τ	$\sqrt{2D_0\tau + 2a^2}$	Width of Gaussian emission after time τ
erfcx(x)	erfc$(x)e^{x^2}$	Scaled complementary error function
$f \star g$	$\int f(\boldsymbol{x})g(\boldsymbol{x}-\boldsymbol{x}')d\boldsymbol{x}'$	A spatial convolution convolution of f and g
$\theta(t)$		Heaviside theta

with

$$\sigma_\tau \equiv \sqrt{2D_0\tau + 2a^2} \tag{A9}$$

(omitting the Heaviside theta with the knowledge that $\tau \geqslant 0$).

The preceding definitions allow us to describe the system of interest in a purely delay-differential form:

$$\frac{d\boldsymbol{r}}{dt} = \int_0^\infty \mathcal{F}(\boldsymbol{r} - \boldsymbol{r}_\tau, \tau)d\tau + \boldsymbol{F}_{\mathbf{ext}}. \tag{A10}$$

Equation (A10) provides a convenient way to test ansatz solutions, as demonstrated in Appendix B. It also forms the basis of the numerical simulations presented in the main text, which use a piecewise polynomial for the history of $r(t-\tau)$ to integrate Eq. (A10).

We note that $\mathcal{F}$ was constructed with Gaussian emission and sensing profiles, $\mathcal{F} \propto \nabla G(0,t) \star N^3(0,a) \star N^3(0,a)$, but the dynamics only depend on $\mathcal{F}$. Therefore, the dynamics are unchanged for any profiles which, when convolved, yield $N^3(0,\sqrt{2}a)$. Notably, this includes $N^3(0,\sqrt{2}a)$ and δ^3, meaning that the same dynamics arise from pointlike sensing and Gaussian emission. This interpretation is useful in both analysis and simulation, as it allows us to write the diffusiophoretic force as a single integral Eq. (A10) over history without singularities. Where necessary to directly calculate the solute density ρ, we can first simulate with Eq. (A10) to generate a trajectory $r(t)$ and then find $\rho(\boldsymbol{x})$ and a point $\boldsymbol{x}$ via Eq. (A6).

APPENDIX B: STEADY-STATE SOLUTIONS

In Appendix A, we derived an expression Eq. (A10) which describes the system as an integrodifferential or delay-differential equation. This relates the time derivative of a particle's position, $\dot{\boldsymbol{r}}$, to a local functional of its prior values $\boldsymbol{r}_\tau$. The dynamics of interest here come from $\boldsymbol{F}_{\text{ext}}$: The various external forces acting on the particle in addition to the gradient of its own emissions. In practice, this may represent a position-dependent force, a time-dependent force or process (e.g., Brownian force), or the solute gradient from other particles.

Here we examine a few special cases of $\boldsymbol{F}_{\text{ext}}$ which are constant in the particle's frame of reference and permit simple solutions for $\boldsymbol{r}(t)$. In doing so, we extract parameters that can be used in constructing a finite-dimensional approximation to the delay-differential equations.

1. Straight-line solutions and spontaneous symmetry breaking

The simplest case we will consider is one where the particle's velocity is constant, which we will denote $\boldsymbol{v}$. This implies a solution of

$$\boldsymbol{r}(t) = \boldsymbol{v}t, \tag{B1}$$

or in the particle's frame of reference a differential equation for ρ:

$$(D_0\nabla^2 + \boldsymbol{v}\cdot\nabla)\rho = -N^3(0,a). \tag{B2}$$

As mentioned previously, for every choice of speed v the history of Eq. (B1) will generate a corresponding steady-state cloud which can be found via Eq. (A6). Likewise, we can find the gradient of ρ at the particle's position, and thus the diffusiophoretic force, via Eq. (A10). Plugging Eq. (B1) into Eq. (A10) gives

$$\boldsymbol{v} = \mu\int_0^\infty \mathcal{F}(\boldsymbol{v}\tau,\tau)d\tau + \boldsymbol{F}_{\text{ext}} \tag{B3a}$$

$$= \mu\int_0^\infty N^3(\boldsymbol{v}\tau,\sigma_\tau)\frac{v_0\tau\hat{\boldsymbol{e}}_x}{\sigma_\tau^2}d\tau + \boldsymbol{F}_{\text{ext}}. \tag{B3b}$$

We note that the integrand in Eq. (B3a), given by Eq. (A8), is always parallel to $\boldsymbol{v}$. From this alone, we can conclude several things:

(1) $\boldsymbol{v} = 0 \Rightarrow \boldsymbol{F}_{\text{ext}} = 0$.
(2) $\boldsymbol{v} \parallel \boldsymbol{F}_{\text{ext}}$.
(3) For any $\boldsymbol{v}$ and μ, $\boldsymbol{F}_{\text{ext}}$ can close Eq. (B3a).
(4) For any $\|\boldsymbol{v}\|$ and $\boldsymbol{F}_{\text{ext}}$, μ can close Eq. (B3a).

Fortunately, Eq. (B3a) can be evaluated directly, reducing to

$$P = \frac{\mu}{8\pi D_0^2 a}\frac{\frac{2P}{\sqrt{\pi}} + (1-P^2)\text{erfcx}(P) - 1}{P^2} + \frac{a}{D_0}\boldsymbol{F}_{\text{ext}}\cdot\widehat{v}, \tag{B4}$$

with

$$P \equiv \frac{va}{D_0} \tag{B5}$$

and

$$\text{erfcx}(P) \equiv \text{erfc}(P)\exp(P^2). \tag{B6}$$

One use for Eq. (B4) is to give an explicit formula for the motility constant μ needed to achieve a desired autonomous swimming speed, given the constants a and D_0:

$$\mu(P) = 8\pi D_0^2 a\frac{P^3}{\frac{2P}{\sqrt{\pi}} + (1-P^2)\text{erfcx}(P) - 1}. \tag{B7}$$

This reveals an important property around $P \to 0^+$, namely,

$$\mu_c = \lim_{P\to 0^+}\mu(P) = 12\pi^{3/2}D_0^2 a, \tag{B8}$$

which defines a critical value μ_c, below which self-sustained motion is not possible.

Equation (B4) can be manipulated to give an explicit expression for the shift in swimming speed due to a small external force at any speed:

$$\lim_{F\to 0}\frac{\partial v}{\partial F} \equiv \alpha + 1 \tag{B9a}$$

$$= \left(3 + 3\frac{\mu}{\mu_c}(\text{erfcx}(P)P\sqrt{\pi} - 1) - 2\frac{F}{v}\right)^{-1} \tag{B9b}$$

$$= \frac{\frac{2P}{\sqrt{\pi}} - (P^2-1)\text{erfcx}(P) - 1}{\frac{2P}{\sqrt{\pi}}(3-P^2) + (2P^4 - 3P^2 + 3)\text{erfcx}(P) - 3}. \tag{B9c}$$

The above is used in the main body as a predictor of the slope of $v_{s,\parallel}$ vs $F_\parallel$ for simulated particles in a random potential.

By expanding around $v = 0$, we find

$$\lim_{v\to 0^+}\frac{dF}{dv} = \left(1 - \frac{\mu}{\mu_c},\right) \tag{B10}$$

which tells us that the $v = 0$ solution is unstable for $\mu > \mu_c$ (a retarding force is required to maintain an infinitesimal speed). It also shows that, in the subcritical regime, the effect of small forces on movement speed are amplified by a factor of $(1 - \mu/\mu_c)^{-1}$. Although this result only strictly holds for constant forces, this would likely cause enhanced diffusion for the low-frequency components of a Brownian force for particles which can't quite swim on their own.

A notable feature arises if we evaluate Eq. (B9) with μ as a function of P, as in Eq. (B7). Then dv/dF diverges at $v = 0$ and decreases monotonically to an asymptote of $1/2$. But since Eq. (B9) represents the *total shift* in swimming velocity, and $v = F_{\text{self}} + F_{\text{ext}}$, the shift in F_{self} asymptotes to $-1/2$. This means that a small, constant external force may enhance or suppress the diffusiophoretic force F_{self}, depending on the system's Péclet number and there exists a value $P \approxeq 1.2577$ where F_{self} has no first-order shift from an external force.

Finally, it is useful to visualize the cloud ρ which surrounds a particle in the moving steady state. Happily, a solution to Eq. (B2) is known in the point-source limit where $a \to 0$, being the description of heat dissipation around a moving weld [24,25]:

$$\rho(\boldsymbol{x}; a \to 0) = \frac{e^{-\boldsymbol{v}\cdot\boldsymbol{x}} e^{-|\boldsymbol{v}||\boldsymbol{x}|}}{4\pi D_0 |\boldsymbol{x}|}. \tag{B11}$$

As mentioned in Appendix A, we may evaluate Eq. (B11) and convolve the result with $N^3(\boldsymbol{x}, a)$ to find the resulting ρ, or with $N^3(\boldsymbol{x}, \sqrt{2}a)$ to find the cloud seen by an equivalent system with pointlike sensing.

2. Circular orbits

Another steady-state solution we may consider is uniform circular motion, with an external force $\boldsymbol{F}_{\text{ext}}$ which is constant in the particle's rotating frame, as could arise from motion in a central potential. Again, we posit a trajectory

$$\boldsymbol{r}(t) = R\widehat{\boldsymbol{e}_r} = \cos(\omega t)\widehat{\boldsymbol{e}_x} + \sin(\omega t)\widehat{\boldsymbol{e}_y} \tag{B12}$$

such that

$$\frac{d\boldsymbol{r}}{dt} = R\omega\widehat{\boldsymbol{e}_\theta} = v\widehat{\boldsymbol{e}_\theta}. \tag{B13}$$

From this hypothesis, the time-delayed displacement is given by

$$\boldsymbol{r} - \boldsymbol{r}_\tau = R((1 - \cos\omega\tau)\widehat{\boldsymbol{e}_r} + \sin(\omega\tau)\widehat{\boldsymbol{e}_\theta}), \tag{B14}$$

and using Eq. (A10) we can relate the hypothesized trajectory's parameters (R and ω) to the motility constant μ and the force $\boldsymbol{F}_{\text{ext}}$ required to make the hypothesis self-consistent. With some manipulation, this becomes

$$F_r = 0 - \frac{\mu R}{\sqrt{2\pi}^3}\int_0^\infty \exp\left[-\left(\frac{R\sin\left(\frac{\omega\tau}{2}\right)}{\sigma_\tau}\right)^2\right]\frac{2\sin\left(\frac{\omega\tau}{2}\right)^2}{\sigma_\tau^5}d\tau, \tag{B15}$$

$$F_\theta = R\omega - \frac{\mu R}{\sqrt{2\pi}^3}\int_0^\infty \exp\left[-\left(\frac{R\sin\left(\frac{\omega\tau}{2}\right)}{\sigma_\tau}\right)^2\right]\frac{\sin(\omega\tau)}{\sigma_\tau^5}d\tau. \tag{B16}$$

These can be integrated numerically, as shown in the main body, to give the resulting radial and tangential components of the external force needed for a particular orbit.

If we expect $\boldsymbol{F}_{\text{ext}}$ to be conservative, then F_θ must vanish. As in the straight-line case, this provides an expression for μ in terms of the expected R and ω. This also provides a way to construct a potential consistent with orbits of *any radius*—by starting from the straight-line values of μ and v, we repeatedly decrease R and adjust v to keep μ constant. This allows us to determine all possible (R, v) pairs permitted by a given system defined by μ, a, and D_0, as well as the centripetal force $F_r(R)$ needed to counteract the radial component of the diffusiophoresis:

$$v(R) = \{R\omega \ni F_\theta(R, \omega; \mu, a, D_0) = 0\}. \tag{B17}$$

We note, however, that these orbits are not all stable, and numerical experiments suggest that a real particle, placed in a potential so constructed, would drift to $R \to \infty$.

Equations (B15) and (B16) can be solved numerically to yield, for a given system, the orbital velocity as a function of radius. Recalling that $v = PD_0/a$, we can see that for a given system parameterized by (μ, D_0, a), Eqs. (B19) and (B20) are functions of R alone.

As with any circular trajectory, the particle's acceleration is, by assertion, v^2/R. We can define a quantity $m^\star(R)$ to be the ratio between this acceleration and required centripetal force F_r:

$$m^\star(R) \equiv \frac{F_r(R; \mu, a, D_0)}{v(R)^2/R}. \tag{B18}$$

Finally, we can again examine the response to a weak external force. We expand Eqs. (B15) and (B16) as deviations from the straight-line trajectory (this requires both $R \gg a$ and $R \gg D_0/v$), which gives

$$F_r \approx \frac{\mu}{8\pi D_0 a^2}\frac{a}{R}\left(\frac{\frac{2P}{\sqrt{\pi}} + \left(1 - 2P^2\right)\text{erfcx}(P) - 1}{2P}\right) + \mathcal{O}(R^{-3}), \tag{B19}$$

$$F_\theta \approx v - \frac{\mu}{8\pi D_0 a^2}\left(\frac{\frac{2P}{\sqrt{\pi}} + \left(1 - P^2\right)\text{erfcx}(P) - 1}{P^2}\right) + \mathcal{O}(R^{-2}). \tag{B20}$$

Noting that the dominant term in Eq. (B19) scales with R^-1, and that $v(R)$ must approach the straight-line solution described in Eq. B 1, one can see that $m^\star$ will approach a constant in the large-R limit. We denote this quantity as $m^\star_\infty$, and its value is

$$\begin{aligned} m^\star_\infty &\equiv \lim_{R\to\infty} m^\star(R) \\ &= \lim_{R\to\infty} \frac{R}{-v^2} F_r(R; \mu, a, D_0) \\ &= \frac{1}{2}\frac{a}{v}\left(\frac{P^3\text{erfcx}(P)}{(1 - P^2)\text{erfcx}(P) + \frac{2P}{\sqrt{\pi}} - 1} - P\right). \end{aligned}$$

The term in parentheses is a function of the dimensionless number, which decreases monotonically from $\frac{3}{2}\frac{\sqrt{\pi}}{2}$ to $\frac{\sqrt{\pi}}{2}$ for $0 < P < \infty$. Note, however, that since $P = va/D_0$, the prefactor of a/v could equivalently be written as PD_0/v^2, along with many other variations.

We can also express the same relation in terms of angular velocity, rather than acceleration, by defining a rotational motility γ_∞ such that $\omega \approx \gamma_\infty F_r$:

$$\gamma_\infty = \frac{2}{a}\left(\frac{-P\mathrm{erfcx}(P)}{\frac{2P}{\sqrt{\pi}} + (1-2P^2)\mathrm{erfcx}(P) - 1} - \frac{1}{P}\right). \tag{B21}$$

[1] N. J. Suematsu and N. Satoshi, Chem. Eur. J. **24**, 6308 (2018).
[2] S. Michelin, E. Lauga, and D. Bartolo, Phys. Fluids **25**, 061701 (2013).
[3] S. Yabunaka, T. Ohta, and N. Yoshinaga, J. Chem. Phys. **136**, 074904 (2012).
[4] S. Thutupalli, R. Seemann, and S. Herminghaus, New J. Phys. **13**, 073021 (2011).
[5] S. Herminghaus, C. C. Maass, C. Krüger, S. Thutupalli, L. Goehring, and C. Bahr, Soft Matter **10**, 7008 (2014).
[6] C. Jin, C. Krüger, and C. C. Maass, Proc. Natl. Acad. Sci. USA **114**, 5089 (2017).
[7] C. C. Maass, C. Krüger, S. Herminghaus, and C. Bahr, Annu. Rev. Condens. Matter Phys. **7**, 171 (2016).
[8] Z. Izri, M. N. van der Linden, S. Michelin, and O. Dauchot, Phys. Rev. Lett. **113**, 248302 (2014).
[9] T. Toyota, N. Maru, M. M. Hanczyc, T. Ikegami, and T. Sugawara, J. Am. Chem. Soc. **131**, 5012 (2009).
[10] P. de Buyl, A. S. Mikhailov, and R. Kapral, Europhys. Lett. **103**, 60009 (2013).
[11] S. Tanaka, Y. Sogabe, and S. Nakata, Phys. Rev. E **91**, 032406 (2015).
[12] H. M. Devaux, La Nature (1888).
[13] W. H. Larrabee, Popular Sci. Mon. **35**, 591 (1889).
[14] H. Boukellal, O. Campás, J.-F. Joanny, J. Prost, and C. Sykes, Phys. Rev. E **69**, 061906 (2004).
[15] G. P. Alexander and A. J. Liu, arXiv:1107.3851.
[16] A. Mikhailov and D. Meinköhn, in *Stochastic Dynamics*, Lecture Notes in Physics (Springer, Berlin, Heidelberg, 1997), pp. 334–345.
[17] See Supplemental Material at http://link.aps.org/supplemental/10.1103/PhysRevE.109.054602 for animations of simulated particle trajectories in randomly generated envrionments.
[18] M. R. Shaebani, A. Wysocki, R. G. Winkler, G. Gompper, and H. Rieger, Nat. Rev. Phys. **2**, 181 (2020).
[19] P. Illien, C. de Blois, Y. Liu, M. N. van der Linden, and O. Dauchot, Phys. Rev. E **101**, 040602(R) (2020).
[20] S. Suda, T. Suda, T. Ohmura, and M. Ichikawa, Phys. Rev. Lett. **127**, 088005 (2021).
[21] A. Izzet, P. G. Moerman, P. Gross, J. Groenewold, A. D. Hollingsworth, J. Bibette, and J. Brujic, Phys. Rev. X **10**, 021035 (2020).
[22] B. V. Hokmabad, R. Dey, M. Jalaal, D. Mohanty, M. Almukambetova, K. A. Baldwin, D. Lohse, and C. C. Maass, Phys. Rev. X **11**, 011043 (2021).
[23] B. V. Hokmabad, J. Agudo-Canalejo, S. Saha, R. Golestanian, and C. C. Maass, Proc. Natl. Acad. Sci. USA **119**, e2122269119 (2022).
[24] D. Rosenthal, Weld J. **20**, 220S (1941).
[25] D. Rosenthal, ASME Trans. **68**, 849 (1946).